Optical Materials: X 12 (2021) 100095

Contents lists available at ScienceDirect

Optical Materials: X

journal homepage: www.journals.elsevier.com/optical-materials-x

Ellipsometric analysis of isothermally devitrified metallic glasses

Ceren Uzun [a,b,*], Chandra Sekhar Meduri [d], Shweta Jagdale [d], Golden Kumar [d], Ayrton A. Bernussi [b,c]

[a] Department of Physics and Astronomy, Texas Tech University, Lubbock, TX, 79409, USA
[b] Nanotech Center, Texas Tech University, Lubbock, TX, 79409, USA
[c] Department of Electrical and Computer Engineering, Texas Tech University, Lubbock, TX, 79409, USA
[d] Department of Mechanical Engineering, The University of Texas at Dallas, Richardson, TX, 75080, USA

ARTICLE INFO

Keywords:
Metallic glasses
Devitrification
Spectroscopic ellipsometry

ABSTRACT

Effects of devitrification in metallic glasses are of particular interest for their utilization in various applications as the phase transformation from amorphous to crystalline state is known to significantly change their properties. In this work, we study the effect of devitrification on the optical properties of metallic glasses using the spectroscopic ellipsometry technique. Ellipsometry measurements on isothermally crystallized samples at controlled temperatures between the glass transition temperature and the crystallization temperature revealed characteristic dependence of the complex index of refraction on the controlled devitrification temperature, suggesting an effective optical approach which can be prospectively used for characterization of structural changes during devitrification. The crystallinity of devitrified samples was verified using a combination of differential scanning calorimetry and X-ray diffraction measurements.

1. Introduction

Metallic glasses (MGs) are a broad family of metal alloys that are specifically designed to prevent crystallization at relatively low cooling rates [1]. They exhibit unique mechanical and thermo-physical properties owing to their metallic and glassy nature including high strength, superior corrosion and wear resistance, and large elastic strain limit [2–5]. Most importantly, MGs show a metastable supercooled liquid state in the temperature range between the glass transition temperature (T_g) and the crystallization temperature (T_x) [4]. The supercooled liquid state enables the MGs to be thermoplastically formed to generate complex geometries and surface patterns spanning from centimeter to nanoscale [2,3,6]. Thermoplastic forming of MGs has been utilized for applications in micro-nano-electromechanical systems [7,8], electrochemical catalysis [9,10], biochemical and biomedical systems [11,12], and photovoltaics [13]. It has been recently demonstrated that low optical reflectance (<2%) in the visible range can be achieved using nanotextured MG surfaces [14]. Also, it has been shown that a localized photo-thermal heat conversion in the near-infrared region can be realized with MG nanowires made by thermoplastic embossing [15,16]. Despite the growing recent interest in MGs for potential applications that involve photo-thermal energy conversion [16,17], and high absorption [14,18], the optical properties of different types of bulk MGs that are suitable for thermoplastic forming remain largely unexplored.

The properties of materials depend on the atomic structure and microstructure besides the surface topology. In our previous study, we demonstrated distinct index of refraction (n) and extinction coefficient (k) of amorphous and crystallized Pt-based MGs [14,19]. Recently, the optical constants of Pd-based amorphous and crystalline glass formers have been reported using spectroscopic ellipsometry (SE) [20]. MGs devitrify into a wide variety of phases and microstructures depending on the crystallization conditions. Considerable efforts have been dedicated to understand the microstructural effects of crystallization on the mechanical properties of MGs [21–23]. However, it remains unclear if the optical properties of devitrified MG formers are also sensitive to the microstructure devitrification conditions. Here, we propose to use SE to investigate the effects of temperature-dependent devitrification of MGs on their optical properties.

To achieve this, we investigated the complex refractive index dispersion relations of MGs that are isothermally crystallized at temperatures between T_g and T_x. The optical properties combined with X-ray diffraction results suggest the formation of distinct microstructures during isothermal annealing. To gain further insight into the properties associated with crystallization, we calculated the complex optical

* Corresponding author. Materials Physics and Applications Division, Los Alamos National Laboratory, Los Alamos, NM, 87545, USA.
E-mail address: ceren@lanl.gov (C. Uzun).

https://doi.org/10.1016/j.omx.2021.100095
Received 31 July 2021; Received in revised form 6 September 2021; Accepted 20 September 2021
Available online 2 October 2021

conductivity of our samples based on the Drude model using the measured complex refractive index dispersion relations. The ability to distinguish the microstructural differences using optical properties provides a new non-destructive characterization technique for MGs that are subjected to heat treatments.

2. Sample fabrication

Amorphous samples of $Pt_{57.5}Cu_{14.7}Ni_{5.3}P_{22.5}$ (Pt-MG) investigated in this study were synthesized by water quenching. Details of the Pt-MG synthesis process can be found elsewhere [3]. All samples were pressed against an ultrasmooth silicon surface during devitrification to achieve a mirror-like surface finish for ellipsometric analysis. Amorphous samples were devitrified by isothermal annealing in the supercooled liquid region based on the time-temperature-transformation (TTT) diagram reported previously [4]. The samples were annealed at temperatures $T_1 = 265$ °C, $T_2 = 270$ °C, and $T_3 = 280$ °C to achieve the crystalline state as per the TTT diagram. The crystallinity of devitrified samples was confirmed using the differential scanning calorimetry (DSC) and X-ray diffraction (XRD) measurements. All our ellipsometric measurements were cross-checked using multiple samples that were prepared using the same surface treatment and devitrification protocol. Measurements in different areas of the same sample revealed no noticeable differences in the complex refractive index indicating excellent macroscopic material uniformity both in amorphous and crystalline states.

3. Spectroscopic ellipsometry

All SE measurements were performed using a Horiba Jobin Yvon UVISEL Ellipsometer (spectral range 250–2100 nm). Light emitted from a Xenon lamp at a fixed 70° angle from the incident plane is collimated into an elliptical spot with major and minor axis lengths of 3.3 mm and 1.0 mm, respectively, at the sample surface. The SE measurements are representative of the entire sample because the beam size is significantly larger than any structural or compositional heterogeneity present in amorphous and crystallized MGs. The fundamental ellipsometry equation is expressed in terms of the intensities of the *p*- and *s*-polarization coefficients of the reflected beam. Ellipsometer angles Δ and Ψ are related to the phase difference and R_p and R_s are the Fresnel reflection amplitude coefficients along the *p*- and *s*-polarization directions, respectively. Measured intensities related to the second (I_s) and the first harmonic (I_c) of the reflected beam can be expressed in terms of the ellipsometer angles Δ and Ψ using the equations $I_s = \sin 2\Psi \sin \Delta$ and $I_c = \sin 2\Psi \cos \Delta$.

To determine the optical constants, a physical model of the material composition and structure was developed. The measured wavelength-dependent intensities I_s and I_c are then fitted to the model to determine the wavelength dispersions of $n(\lambda)$ and $k(\lambda)$. In the SE analysis of both amorphous and devitrified MG samples, we used the Drude model in which the frequency-dependent complex dielectric function $\varepsilon(\omega)$ is given by:

$$\varepsilon(\omega) = \varepsilon_\infty - \frac{\omega_p^2}{\omega^2 + i\omega\Gamma_D} \quad (1)$$

where ε_∞ is the dielectric constant in the high-frequency limit, ω_p is the plasma frequency, Γ_D is the free electron damping factor, and $\varepsilon(\omega) = [n(\omega) + ik(\omega)]^2$.

4. Results and discussion

After measuring the parameters I_s and I_c of the Pt-MG in the amorphous state, the sample was devitrified by annealing at $T_3 = 280$ °C for ~15 min. A second SE measurement was performed on the same sample in the crystalline state after devitrification. The Drude parameters determined for the amorphous and the crystalline states were $\varepsilon_\infty = 1.2$ eV and 1.5 eV, $\omega_p = 22$ eV and 25 eV, and $\Gamma_D = 15.2$ eV and 13.5 eV, respectively, and they are in good agreement with previously reported values for Pt-MGs [14]. Variation in Drude parameters among the devitrified samples was determined to be <6% based on our model.

In order to investigate the microstructural dependence of *n* and *k* dispersions, we compared Pt-MG samples devitrified at three different temperatures [4]. Fig. 1 shows the DSC curves of Pt-MG samples after devitrification at 265 °C, 270 °C, and 280 °C. The DSC curve of amorphous sample is also shown for comparison. The T_g and T_x are clearly visible in the amorphous sample whereas no such transitions are observed in the devitrified samples. A small exothermic event remains in the range of 310–320 °C. It is known that 100% crystalline state is typically not observed in isothermally annealed MGs over laboratory timescales [24]. However, for all practical purposes, the three samples can be considered crystalline with no apparent difference. This assumption can be further verified using the XRD analysis of the devitrified samples.

The XRD patterns of the Pt-MG samples devitrified at different temperatures are shown in Fig. 2. All three samples exhibited sharp diffraction peaks with no diffuse background corresponding to a significant residual amorphous phase. Therefore, the volume of remaining amorphous phase causing the exothermic event in the DSC curves should be less than 5% detectable limit of XRD. Furthermore, the diffraction peaks are identical in all three samples suggesting the formation of the same crystalline phases. A slight narrowing of the diffraction peaks with increasing devitrification temperature is noticeable which is typical in MGs due to formation of coarse grains at higher temperature. Overall, the DSC and XRD results indicate that the isothermal devitrification of Pt-MG at three different temperatures results in formation of the same phases but different microstructures.

The corresponding *n* and *k* wavelength dispersions for both amorphous and devitrified Pt-MGs are shown in Fig. 3. Both the index of refraction (*n*) and the extinction coefficient (*k*) for amorphous and crystalline Pt-MGs exhibit a featureless monotonic increase in the investigated wavelength range. The transition from amorphous to crystalline state results in structural heterogeneity and periodicity. Thus, higher *n* and *k* values observed in the crystalline states likely stem from the higher mass density due to crystallization into an ordered structure from a liquid-like disordered structure as a result of localized changes in composition, as reported in previous investigations [14,20]. Another

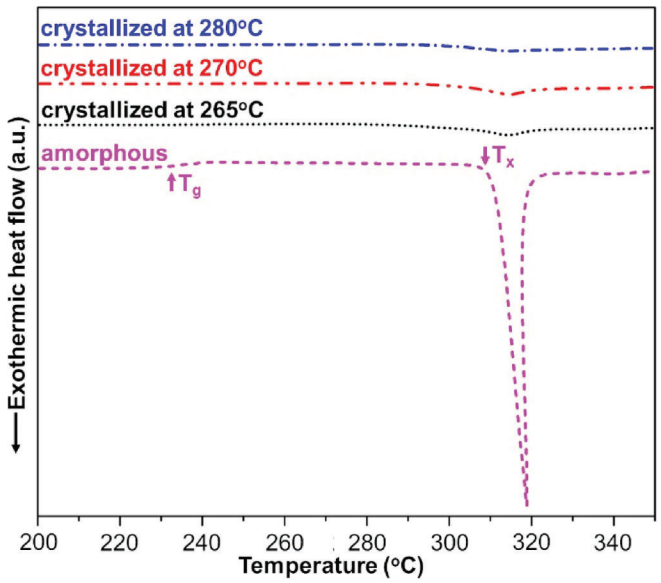

Fig. 1. DSC thermogram for amorphous Pt-MG and the Pt-MGs crystallized at temperatures $T_1 = 265$ °C, $T_2 = 270$ °C, and $T_3 = 280$ °C.

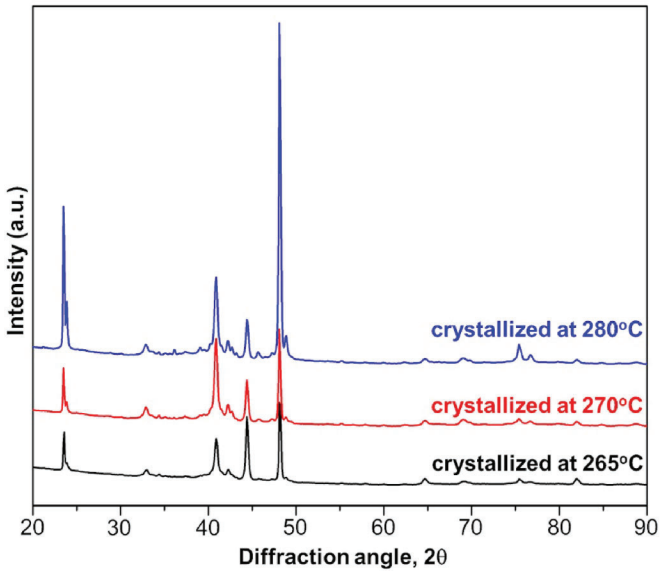

Fig. 2. XRD patterns of the Pt-MGs crystallized at temperatures $T_1 = 265$ °C, $T_2 = 270$ °C, and $T_3 = 280$ °C.

distinct trend observed in Fig. 3 is that, both n and k increase throughout the entire spectrum as the devitrification temperature is increased. This may be attributed to the relation between the size of grain formation and the temperature during devitrification as shown in previous studies [25–29]. Pt-MG in the crystalline state is comprised of many crystalline phases of different sizes that are developed within the amorphous matrix and are separated by disordered grain boundaries [30]. At lower crystallization temperatures, the formation of smaller grains likely results in a volumetric increase of the grain boundaries and a degree of disorder in the structure. As the crystallization temperature is increased, the formation of larger grains leads to a higher effective optical constant for the medium as has been observed in our ellipsometric analysis [31]. Thus, different crystallization temperatures result in the formation of distinct microstructures according to which different optical responses are revealed among the investigated samples.

To further understand the effects of devitrification on the material properties, we have calculated the complex optical conductivity of samples crystallized at different temperatures. The frequency-dependent complex dielectric function $\varepsilon(\omega)$ can be expressed in terms of the complex optical conductivity $\sigma(\omega)$ based on the Drude model using the equation:

$$\varepsilon(\omega) = 1 + i\frac{\sigma(\omega)}{\omega\varepsilon_0} \tag{2}$$

where $\sigma(\omega) = \sigma_r(\omega) + i\sigma_i(\omega)$ and σ_r and σ_i represent the real and imaginary part of the optical conductivity, respectively. The calculated values of σ_r and σ_i for the amorphous and crystallized Pt-MG samples are shown in Fig. 4(a) and (b). The real parts of the optical conductivities exhibit featureless and monotonic curves that increase with the increasing devitrification temperature. Distinct conduction responses among the crystalline samples may also be rationalized in terms of temperature-dependent microstructure formation upon crystallization [32]. While crystallization introduces structural periodicity and homogeneity compared to disordered amorphous Pt-MG, emerging crystal grains limit electron mobility due to scattering from the boundaries. As the crystallization temperature is increased, the formation of larger grains results in a higher degree of order and smoother grain boundaries within the structure that leads to higher conductivity.

The real optical conductivity values are known to be in good agreement with the DC conductivity values in the higher wavelengths of the spectrum for conducting materials. Since we have limited our spectral range to 2100 nm in our SE analysis, we measured the DC resistivity of both amorphous and crystalline samples using the conventional 4-point probe technique. Our resistivity measurements for amorphous Pt-MGs are in good agreement with the known value reported elsewhere [33] and are consistently higher than of isothermally crystallized Pt-MGs due to increased scattering of the conduction electrons from the disordered structure [34].

5. Conclusions

We have investigated the dispersion relations of Pt-MGs in the amorphous and devitrified states using the SE technique. The higher optical constants of devitrified Pt-MG compared to the amorphous Pt-MG are attributed to the higher material density in the crystalline state due to the formation of structural order upon crystallization. We further expanded our spectroscopic analysis to the Pt-MGs that are devitrified isothermally at different temperatures. Our SE measurements showed that the dispersion relations obtained from these samples exhibit similar monotonic curves but distinct n and k dispersion values that increase with increasing devitrification temperature. We calculated the complex optical conductivity of both amorphous and crystallized Pt-MGs based on the Drude model using the measured complex index of refraction values. The dependence of the optical constants and conductivities on the crystallization temperature is attributed to the formation of different sizes of crystal grains during devitrification. We anticipate that the crystallization temperature dependence of the dispersion relations of Pt-MGs can potentially be utilized as a complementary method to study the microstructural effects of devitrification for MGs.

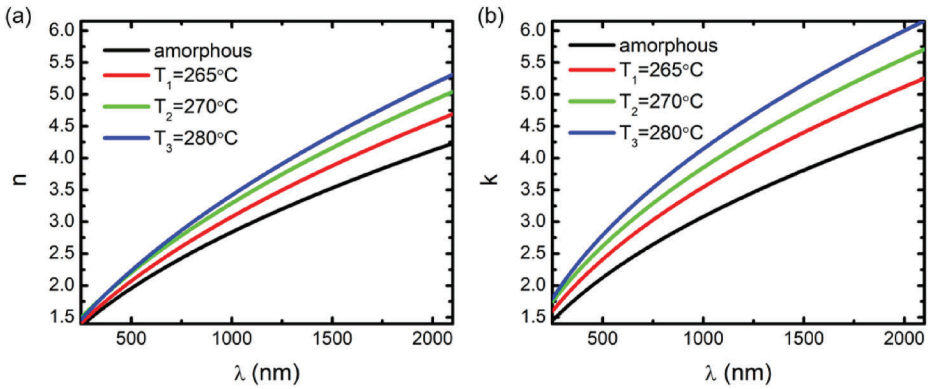

Fig. 3. (a) Index of refractions and (b) extinction coefficients as a function of wavelength for the amorphous Pt-MG and the Pt-MGs crystallized at temperatures $T_1 = 265$ °C, $T_2 = 270$ °C, and $T_3 = 280$ °C.

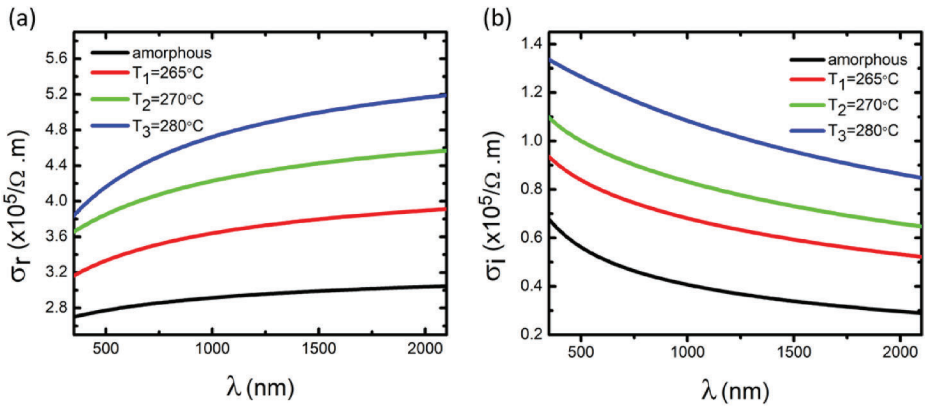

Fig. 4. (a) Real and (b) imaginary parts of complex optical conductivity as a function of wavelength for the amorphous Pt-MG and the Pt-MGs crystallized at temperatures $T_1 = 265$ °C, $T_2 = 270$ °C, and $T_3 = 280$ °C.

CRediT authorship contribution statement

Ceren Uzun: Methodology, Validation, Formal analysis, Investigation, Visualization, Writing – original draft. **Chandra Sekhar Meduri:** Validation, Investigation, Resources, Data curation, Visualization. **Shweta Jagdale:** Validation, Investigation, Resources, Data curation, Visualization. **Golden Kumar:** Methodology, Conceptualization, Writing – review & editing, Supervision, Project administration, Funding acquisition. **Ayrton A. Bernussi:** Methodology, Conceptualization, Writing – review & editing, Supervision, Project administration, Funding acquisition.

Declaration of competing interest

The authors declare that they have no known competing financial interests or personal relationships that could have appeared to influence the work reported in this paper.

Acknowledgements

GK acknowledges the support from the National Science Foundation (NSF) through CMMI Award#1919445 and NSF-CAREER Award#1921435.

References

[1] M. Chen, A brief overview of bulk metallic glasses, NPG Asia Mater. 3 (2011) 82–90, https://doi.org/10.1038/asiamat.2011.30.
[2] G. Kumar, H.X. Tang, J. Schroers, Nanomoulding with amorphous metals, Nature 457 (2009) 868–872, https://doi.org/10.1038/nature07718.
[3] G. Kumar, A. Desai, J. Schroers, Bulk metallic glass: the smaller the better, Adv. Mater. 23 (2011) 461–476, https://doi.org/10.1002/adma.201002148.
[4] J. Schroers, W.L. Johnson, Highly processable bulk metallic glass-forming alloys in the Pt-Co-Ni-Cu-P system, Appl. Phys. Lett. 84 (2004) 3666–3668, https://doi.org/10.1063/1.1738945.
[5] J.F. Löffler, Bulk metallic glasses, Intermetallics 11 (2003) 529–540, https://doi.org/10.1016/S0966-9795(03)00046-3.
[6] M. Hasan, J. Schroers, G. Kumar, Functionalization of metallic glasses through hierarchical patterning, Nano Lett. 15 (2015) 963–968, https://doi.org/10.1021/nl504694s.
[7] R.C. Sekol, G. Kumar, M. Carmo, F. Gittleson, N. Hardesty-dyck, S. Mukherjee, J. Schroers, A.D. Taylor, Bulk metallic glass micro fuel cell, Small 9 (2013) 2081–2085.
[8] M. Kanik, P. Bordeenithikasem, G. Kumar, E. Kinser, J. Schroers, High quality factor metallic glass cantilevers with tunable mechanical properties, Appl. Phys. Lett. 105 (2015), https://doi.org/10.1063/1.4897305.
[9] R.C. Sekol, M. Carmo, G. Kumar, F. Gittleson, G. Doubek, K. Sun, J. Schroers, D. Taylor, Pd - Ni - Cu - P metallic glass nanowires for methanol and ethanol oxidation in alkaline media, Int. J. Hydrogen Energy 38 (2013) 11248–11255, https://doi.org/10.1016/j.ijhydene.2013.06.017.
[10] S. Mukherjee, R.C. Sekol, M. Carmo, E.I. Altman, A.D. Taylor, J. Schroers, Tunable hierarchical metallic-glass nanostructures, Adv. Funct. Mater. 23 (2013) 2708–2713.
[11] J. Li, F.S. Gittleson, Y. Liu, J. Liu, A.M. Loye, L. McMillon-Brown, T.R. Kyriakides, J. Schroers, A.D. Taylor, Exploring a wider range of Mg-Ca-Zn metallic glass as biocompatible alloys using combinatorial sputtering, Chem. Commun. 53 (2017) 8288–8291, https://doi.org/10.1039/C7CC02733H.
[12] J. Schroers, G. Kumar, T.M. Hodges, S. Chan, T.R. Kyriakides, Bulk metallic glasses for biomedical applications, J. Occup. Med. 61 (2009) 21–29, https://doi.org/10.1007/s11837-009-0128-1.
[13] J.P. Singer, M. Gopinadhan, Z. Shao, A.D. Taylor, J. Schroers, C.O. Osuji, Nanoimprinting Sub-100 nm features in a photovoltaic nanocomposite using durable bulk metallic glass molds, ACS Appl. Mater. Interfaces 7 (2015) 3456–3461.
[14] H.J. Tarigan, N. Kahler, N.S. Ramos, G. Kumar, A.A. Bernussi, Low reflectance of nano-patterned Pt-Cu-Ni-P bulk metallic glass, Appl. Phys. Lett. 107 (2015), https://doi.org/10.1063/1.4926873.
[15] C. Uzun, N. Kahler, L.G. De Peralta, G. Kumar, A.A. Bernussi, Photo-induced-heat localization on nanostructured metallic glasses, J. Appl. Phys. 122 (2017) 1–6, https://doi.org/10.1063/1.5000682.
[16] C. Uzun, C. Meduri, N. Kahler, L.G. de Peralta, J.M. McCollum, M. Pantoya, G. Kumar, A.A. Bernussi, Photoinduced heat conversion enhancement of metallic glass nanowire arrays, J. Appl. Phys. 125 (2018) 15102, https://doi.org/10.1063/1.5059423.
[17] C. Uzun, Optical, Thermal and Crystallization Characteristics of Metallic Glasses, 2020.
[18] Z. Hu, C. Uzun, Z. Dong, W. Li, A.A. Bernussi, G. Kumar, Elastocapillary bundling of high aspect-ratio metallic glass nanowires, Appl. Phys. Lett. 111 (2017), https://doi.org/10.1063/1.4993599.
[19] H.J. Tarigan, Ultra-low Optical Scattering with Nano-Structured Bulk Metallic Glasses, Texas Tech University, 2016.
[20] L. McMillon-Brown, P. Bordeenithikasem, F. Pinnock, J. Ketkaew, A.C. Martin, J. Schroers, A.D. Taylor, Measured optical constants of Pd77.5Cu6Si16.5 bulk metallic glass, Opt. Mater. X 1 (2019) 100012, https://doi.org/10.1016/j.omx.2019.100012.
[21] C.A. Schuh, T.C. Hufnagel, U. Ramamurty, Mechanical behavior of amorphous alloys, Acta Mater. 55 (2007) 4067–4109, https://doi.org/10.1016/j.actamat.2007.01.052.
[22] R. Busch, The Thermophysical Properties of Bulk Metallic Glass-Forming Liquids, 52, 2000, pp. 39–42.
[23] A.L. Greer, A.L. Greer, Metallic Glasses, 267, 1995, pp. 1947–1953.
[24] B.A. Legg, J. Schroers, R. Busch, Thermodynamics, kinetics, and crystallization of Pt57.3Cu14.6Ni5.3P22.8 bulk metallic glass, Acta Mater. 55 (2007) 1109–1116, https://doi.org/10.1016/j.actamat.2006.09.024.
[25] A. Pratap, A.T. Patel, H.R. Shevde, K.N. Lad, Grain size limit of nanocrystalline materials obtained by annealing bulk metallic glasses, Trans. Indian Ceram. Soc. 71 (2012) 219–221, https://doi.org/10.1080/0371750X.2013.772734.
[26] T. Kulik, Nanocrystallization of metallic glasses, J. Non-Cryst. Solids 287 (2001) 145–161, https://doi.org/10.1016/S0022-3093(01)00627-5.
[27] J. Saida, M. Matsushita, C. Li, A. Inoue, Comparative study of grain growth behavior from a supercooled liquid region of Zr65Cu27.5Al7.5 and Zr65Cu35 metallic glasses, J. Mater. Sci. 35 (2000) 3539–3546, https://doi.org/10.1023/A:1004805328058.
[28] K. Kajiwara, M. Ohnuma, D.H. Ping, O. Haruyama, K. Hono, Nanocrystallization of Pd74Si18Au8 metallic glass, Intermetallics 10 (2002) 1053–1060, https://doi.org/10.1016/S0966-9795(02)00159-0.
[29] B.S. Murty, D.H. Ping, M. Ohnuma, K. Hono, Nanoquasicrystalline phase formation in binary Zr-Pd and Zr-Pt alloys, Acta Mater. 49 (2001) 3453–3462, https://doi.org/10.1016/S1359-6454(01)00254-3.
[30] S. Mridha, D.L. Jaeger, H.S. Arora, R. Banerjee, S. Mukherjee, Atomic distribution in catalytic amorphous metals, J. Nanomater. (2015) 2015, https://doi.org/10.1155/2015/632138.
[31] G.A. Niklasson, C.G. Granqvist, O. Hunderi, Effective medium models for the optical properties of inhomogeneous materials, Appl. Opt. 20 (1981) 26–30, https://doi.org/10.1364/AO.20.000026.

[32] H. Lou, Z. Zeng, F. Zhang, S. Chen, P. Luo, X. Chen, Y. Ren, V.B. Prakapenka, C. Prescher, X. Zuo, T. Li, J. Wen, W.H. Wang, H. Sheng, Q. Zeng, Two-way tuning of structural order in metallic glasses, Nat. Commun. 11 (2020), https://doi.org/10.1038/s41467-019-14129-7.

[33] J.-Y. Suh, Fracture Toughness Study on Bulk Metallic Glasses and Novel Joining Method Using Bulk Metallic Glass Solder, 2009.

[34] J.S. Dugdale, Electron transport in metallic glasses, Contemp. Phys. 28 (1987) 547–572, https://doi.org/10.1080/00107518708213743.